Unsteady effects in flows past stationary airfoils with Gurney flaps due to unsteady flow separations at low Reynolds numbers

Dan MATEESCU*

*Corresponding author
Doctor Honoris Causa, Fellow CASI, Associate Fellow AIAA, Erskine Fellow
Professor Emeritus, Mechanical Engineering Department, McGill University,
Montreal, QC, Canada
dan.mateescu@mcgill.ca

DOI: 10.13111/2066-8201.2015.7.4.11

Received: 23 October 2015 / Accepted: 15 November 2015

The 36th "Caius Iacob" Conference on Fluid Mechanics and its Technical Applications
29 - 30 October, 2015, Bucharest, Romania, (held at INCAS, B-dul Iuliu Maniu 220, sector 6)
Plenary lecture

Abstract*: This paper presents the analysis of the unsteady flows past stationary airfoils equipped with Gurney flaps at low Reynolds numbers, aiming to study the unsteady behavior of the aerodynamic coefficients due to the flow separations occurring at these Reynolds numbers. The Gurney flaps are simple but very efficient lift-increasing devices, which due to their mechanical simplicity are of particular interest for the small size micro-air-vehicles (MAV) flying at low speed and very low Reynolds number. The unsteady aerodynamic analysis is performed with an efficient time-accurate numerical method developed for the solution of the Navier-Stokes equations at low Reynolds numbers, which is second-order-accurate in time and space. The paper presents solutions for the unsteady aerodynamic coefficients of lift and drag and for the lift-to-drag ratio of several symmetric and cambered airfoils with Gurney flaps. It was found that although the airfoil is considered stationary, starting from a relatively small incidence (about 8 degrees) the flow becomes unsteady due to the unsteadiness of the flow separations occurring at low Reynolds numbers, and the aerodynamic coefficients display periodic oscillations in time. A detailed study is presented in the paper on the influence of various geometric and flow parameters, such as the Gurney flap height, Reynolds number, airfoil relative thickness and relative camber, on the aerodynamic coefficients of lift, drag and lift-to-drag ratio. The flow separation is also studied with the aid of flow visualizations illustrating the changes in the flow pattern at various moments in time.*

2000 Mathematics Subject Classification*: 76, 76G25, 76D05, 76M20, 65M06, 35Q30*

Key Words*: Unsteady flows, Low Reynolds number, Subsonic Aerodynamics, Computational Aerodynamics, Viscous Flows*

1. INTRODUCTION

The Gurney flap is a mechanically simple lift-increasing device, consisting of a small tab attached at the trailing edge of an airfoil (or wing), on its pressure side, and perpendicular to its chord. Originally installed by Dan Gurney in early 1970s on the rear inverted wing of a racing car, the Gurney flap was proven to increase the wing lift, which is usually associated

with a small increase of its drag, resulting in a significant increase of its lift-to-drag ratio, when the flap height is only a small percentage (1% to 4%) of the wing chord. The lift increase is mainly due to the fact that the Gurney flap increases the effective camber of the airfoil and decelerates the flow on the lower side, while accelerating the flow on the upper side. In addition to its beneficial effect on the aerodynamic performance of the wing, this device has the advantage of a very low manufacturing and maintenance cost.

For these reasons, Gurney flaps have been thoroughly studied by many authors. Liebeck [1] first found that a Gurney flap installed on the inverted rear wing of a car increased substantially its lift and the racing car performance. Numerical solutions have also been obtained for airfoils with Gurney flaps and they were found in good agreement with the experimental results. Jang [2] has shown that for some configurations, such as a NACA 4412 airfoil with a 1.25% Gurney flap, the lift is higher and the drag is lower than for the airfoil without flap. However, for large size flaps, the aerodynamic performance is compromised by a large increase in drag. It has been shown that for optimal use, the flap height should be in the range of 1% to 4% of the airfoil chord [3].

Recently, some experimental studies have shown that the positive aerodynamic effects of Gurney flaps can be enhanced by using perforated flaps or combining them with harmonically deflected trailing edge flaps [4, 5].

All the above studies have been performed for relatively large Reynolds numbers. However, due to its mechanical simplicity, the utilization of Gurney flap is of particular interest for the small size micro-air-vehicles (MAV) flying at low speed, for which the Reynolds number is between 600 and 6000.

Several studies on the steady flows past airfoils without flaps at low Reynolds number have been published by Kunz & Kroo [6], and Mateescu & Abdo [7, 8] for airfoils in free flight, and by Mateescu *et al* [9] for airfoils in the proximity of the ground.

The unsteady flows past airfoils without flap executing pitching oscillations at low Reynolds numbers has been recently studied by Mateescu *et al*. [10] by using an efficient time-accurate method. The unsteady flow at low Reynolds numbers past oscillating airfoils in the proximity of the ground has been studied by Mateescu *et al*. [11].

More recently, Mateescu *et al*. [12] have studied the unsteady effects on stationary airfoils that are generated by the unsteady flow separations developed at low Reynolds numbers. It was found that starting from relatively small angles of attack (6 or 8 degrees) the aerodynamic coefficients become unsteady due to the unsteadiness of the flow separations at low Reynolds numbers. The new numerical method has been validated by comparison with experiments.

The first attempt to study the effect of Gurney flaps in steady flows at low Reynolds numbers has been published by Dumitrescu & Malael [13], which calculated the steady lift and drag coefficients for the NACA 4404 airfoil at angles of attack up to 8 degrees, for several flap sizes by using a steady flow solver.

The present study is dedicated to the analysis of the unsteady flows past airfoils equipped with Gurney flaps at low Reynolds numbers, aiming to study the unsteady behavior of the aerodynamic coefficients due to the flow separations occurring at these Reynolds numbers. This analysis is performed with an efficient time-accurate numerical method developed by the author for the solution of the unsteady Navier-Stokes equations at low Reynolds numbers, which is second-order-accurate in time and space. A second-order three-point-backward implicit scheme is used first for the real time discretization, followed by a pseudo-time relaxation procedure using artificial compressibility and a factored Alternating Direction Implicit (ADI) scheme for the pseudo-time integration. A second order central

finite difference formulation is used on a stretched staggered grid (which avoids the odd-and-even points decoupling). A special decoupling procedure using the continuity equation reduces the problem to the solution of scalar tridiagonal systems of equations, which enhances substantially the computational efficiency of the method. Solutions for the lift and drag coefficients and for the lift-to-drag ratio are presented for several symmetric and cambered NACA airfoils equipped with Gurney flaps at different Reynolds numbers.

At somewhat larger angles of attack (above 8 degrees, depending on the airfoil geometry and flap size), the lift and drag coefficients display oscillations in time which are generated by the unsteady flow separations developed at low Reynolds numbers. The influence of various geometric and flow parameters, such as the flap size, Reynolds number, angle of attack and the airfoil relative thickness and camber, is also studied in this paper.

2. PROBLEM FORMULATION

Consider a cambered airfoil of chord c placed at an incidence α in a uniform stream of velocity U_∞, as shown in Figure 1. The airfoil, which is equipped with a Gurney flap of height cl, is referred to a Cartesian reference system of coordinates cx, cy, where x and y are nondimensional coordinates (with respect to the chord c), with the *x*-axis along the airfoil chord and its origin at the airfoil leading edge. The airfoil upper and lower surfaces are defined by the equations

$$y = e_1(x) = h(x) + e(x) \qquad \text{and} \qquad y = -e_2(x) = h(x) - e(x), \tag{1}$$

where the subscripts 1 and 2 refer to the upper and lower surfaces, and where $h(x)$ and $e(x)$ define, respectively, the camberline and the airfoil thickness variation along the airfoil chord. The special case of symmetric airfoils is characterized by $e_1(x) = e_2(x) = e(x)$ and $h(x) = 0$. The viscous fluid flow past the oscillating airfoil is referred to a fixed Cartesian reference system of coordinates $c\xi$, $c\eta$ defined by the equations

$$\xi = x\cos\alpha + y\sin\alpha, \quad \eta = -\sin\alpha + y\cos\alpha, \tag{2}$$

where ξ and η are nondimensional coordinates with respect to the airfoil chord c, with the ξ-axis parallel to the uniform stream velocity U_∞, which is inclined with the angle α with respect to the airfoil chord (as shown in Figure 1).

Let $U_\infty u$ and $U_\infty v$ denote the fluid velocity components along the fixed ξ- and η-axes, where u and v are the nondimensional velocity components with respect to U_∞.

The time-dependent Navier-Stokes and continuity equations for the incompressible flow past the airfoil can be expressed in nondimensional conservation form as

$$\frac{\partial \mathbf{V}}{\partial t} + \mathbf{Q}(\mathbf{V}, p) = \mathbf{0}, \qquad \nabla \bullet \mathbf{V} = \frac{\partial u}{\partial \xi} + \frac{\partial v}{\partial \eta} = 0, \tag{3}$$

where $t = t^* U_\infty / c$ is the nondimensional time (t^* is the dimensional time), $\mathbf{V} = \{u, v\}^{\mathrm{T}}$ represents the vector of the dimensionless velocity components and $\mathbf{Q}(\mathbf{V}, p)$, which includes the convective derivative, pressure and viscous terms, can be expressed in 2-D Cartesian coordinates in the form

$$\mathbf{Q}(\mathbf{V}, p) = \{Q_u(u, v, p), Q_v(u, v, p)\}^{\mathrm{T}}, \tag{4}$$

$$Q_u(u,v,p)=\frac{\partial(uu)}{\partial\xi}+\frac{\partial(vu)}{\partial\eta}+\frac{\partial p}{\partial\xi}-\frac{1}{\mathrm{Re}}\left(\frac{\partial^2 u}{\partial\xi^2}+\frac{\partial^2 u}{\partial\eta^2}\right), \tag{5a}$$

$$Q_v(u,v,p)=\frac{\partial(uv)}{\partial\xi}+\frac{\partial(vv)}{\partial\eta}+\frac{\partial p}{\partial\eta}-\frac{1}{\mathrm{Re}}\left(\frac{\partial^2 v}{\partial\xi^2}+\frac{\partial^2 v}{\partial\eta^2}\right), \tag{5b}$$

where p is the dimensionless pressure, nondimensionalized with respect to $\rho U_\infty{}^2$, and $\mathrm{Re}=cU_\infty/\nu$ is the Reynolds number based on the chord length (ρ and ν are the fluid density and kinematic viscosity).

In the present computational analysis we focus our attention on flows at low Reynolds numbers, in which the viscous effects play a very important role.

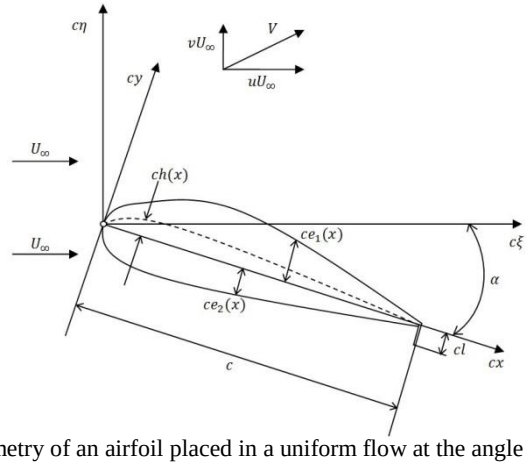

Figure 1. Geometry of an airfoil placed in a uniform flow at the angle of attack α.

The problem is solved in a rectangular computational domain with six sub-domains, which is obtained from the physical domain indicated in Figure 2 by a geometrical transformation defined as

$$X=g(\xi,\eta), \qquad Y=f(\xi,\eta), \tag{6}$$

where $g(\xi,\eta)$ and $f(\xi,\eta)$ are defined for each domain in the following forms.

Domain 1 (for $x<0$ and $0<\eta<H_1$): $g(\xi,\eta)=\dfrac{\xi\cos\alpha-\eta\sin\alpha}{L_0\cos\alpha+\eta\sin\alpha}L_0$, $f(\xi,\eta)=\eta$, (7a)

Domain 2 (for $x<0$ and $-H_2<\eta<0$): $g(\xi,\eta)=\dfrac{\xi\cos\alpha-\eta\sin\alpha}{L_0\cos\alpha+\eta\sin\alpha}L_0$, $f(\xi,\eta)=\eta$, (7b)

Domain 3 (for $0<x<1$ and $e_1(x)<y<H_1$):

$$g(\xi,\eta)=\xi\cos\alpha-\eta\sin\alpha, \qquad f(\xi,\eta)=\frac{y-e_1(x)}{H_1-e_1(x)\cos\alpha+x\sin\alpha}H_1\cos\alpha, \tag{7c}$$

Domain 4 (for $0<x<1$ and $-H_2<y<-e_2(x)$):

$$g(\xi,\eta)=\xi\cos\alpha-\eta\sin\alpha, \qquad f(\xi,\eta)=\frac{y+e_2(x)}{H_2-e_2(x)\cos\alpha-x\sin\alpha}H_2\cos\alpha, \tag{7d}$$

Domain 5 (for $x>1$ and $-\sin\alpha<\eta<H_1$):

$$g(\xi,\eta)=\frac{\xi\cos\alpha-\eta\sin\alpha-1}{L_1\cos\alpha-\eta\sin\alpha-1}(L_1-1)+1, \qquad f(\xi,\eta)=\frac{\eta+\sin\alpha}{H_1+\sin\alpha}H_1, \tag{7e}$$

Domain 6 (for $x>1$ and $-H_2<\eta<-\sin\alpha$):

$$g(\xi,\eta)=\frac{\xi\cos\alpha-\eta\sin\alpha-1}{L_1\cos\alpha-\eta\sin\alpha-1}(L_1-1)+1, \qquad f(\xi,\eta)=\frac{\eta+\sin\alpha}{H_2-\sin\alpha}H_2, \tag{7f}$$

In equations (7), $\eta=H_1$ and $\eta=-H_2$ are the nondimensional physical coordinates of the upper and lower far-field boundaries of the computational domain (which are considered equal in the specific numerical applications presented further, $H_1=H_2=H$), while $\xi=-L_0$ and $\xi=L_1$ are the nondimensional physical coordinates of the inflow and outflow boundaries, as shown in Figure 2.

In the computational domain (X,Y), the upstream inflow and downstream outflow boundaries and the upper and lower boundaries are defined by the same nondimensional coordinates $X=-L_0$, $X=L_1$ and $Y=H_1$, $Y=-H_2$, respectively. The height of the Gurney flap in the computational domain is $\lambda=l\,(H_2\cos\alpha)/(H_2-\sin\alpha)$, that is $Y_l=-\lambda$.

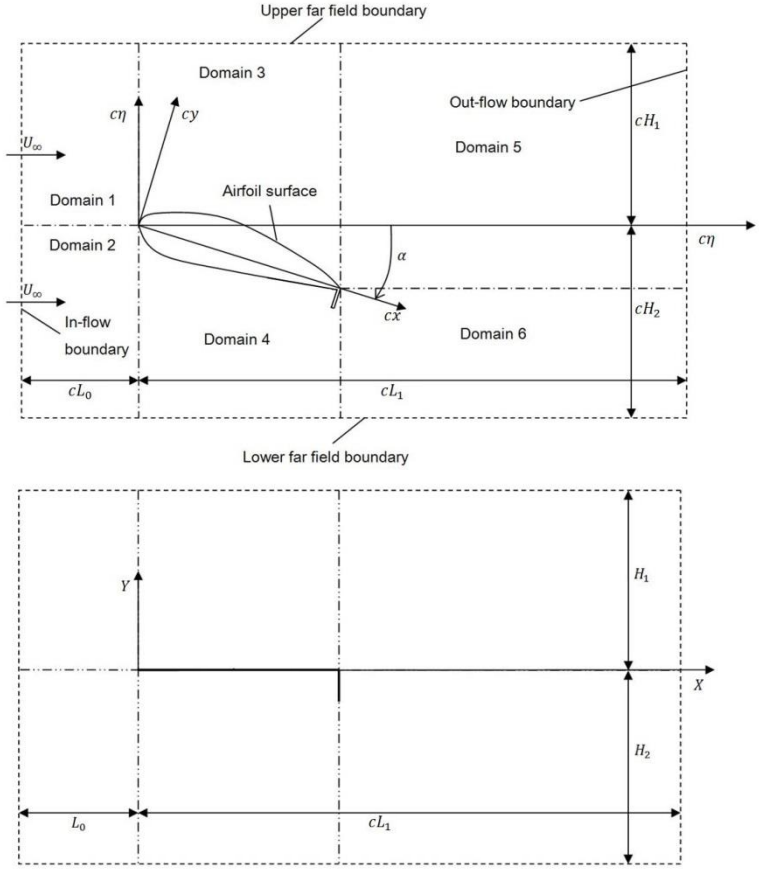

Figure 2. Geometry of the computational domain (X,Y) defined by the transformations (6)-(7).

The Navier-Stokes and continuity equations can be expressed in the computational domain, as

$$\frac{\partial\mathbf{V}}{\partial t}+\mathbf{G}(\mathbf{V},p)=\mathbf{0}\ , \qquad D\mathbf{V}=0\ , \tag{8}$$

where

$$\mathbf{V}=\{u,v\}^{\mathrm{T}},\qquad \mathbf{G}(\mathbf{V},p)=\{G_u(u,v,p),G_v(u,v,p)\}^{\mathrm{T}}, \tag{9}$$

$$\begin{aligned}G_u(u,v,p)&=C_7\frac{\partial(uu)}{\partial X}+C_2\frac{\partial(uu)}{\partial Y}+C_4\frac{\partial(vu)}{\partial X}+C_3\frac{\partial(vu)}{\partial Y}\\&+C_7\frac{\partial p}{\partial X}+C_2\frac{\partial p}{\partial Y}+C_1\frac{\partial^2 u}{\partial X^2}+C_6\frac{\partial^2 u}{\partial X\partial Y}+C_5\frac{\partial^2 u}{\partial Y^2}\end{aligned} \tag{10}$$

$$\begin{aligned}G_v(u,v,p)&=C_7\frac{\partial(vu)}{\partial X}+C_2\frac{\partial(vu)}{\partial Y}+C_4\frac{\partial(vv)}{\partial X}+C_3\frac{\partial(vv)}{\partial Y}\\&+C_4\frac{\partial p}{\partial X}+C_3\frac{\partial p}{\partial Y}+C_1\frac{\partial^2 v}{\partial X^2}+C_6\frac{\partial^2 v}{\partial X\partial Y}+C_5\frac{\partial^2 v}{\partial Y^2}\end{aligned} \tag{11}$$

$$D\mathbf{V}=C_7\frac{\partial u}{\partial X}+C_2\frac{\partial u}{\partial Y}+C_4\frac{\partial v}{\partial X}+C_3\frac{\partial v}{\partial Y}, \tag{12}$$

in which the expressions of the coefficients C_1, C_2, . . . , C_7 are obtained for each domain from the coordinate transformations (6) - (7).

In order to study the unsteady flow past stationary airfoils with Gurney flaps at low Reynolds numbers, the Navier-Stokes momentum equation is first discretized in real time based on a second-order three-point-backward implicit scheme:

$$\left(\frac{\partial\mathbf{V}}{\partial t}\right)^{n+1}=\frac{3\mathbf{V^{n+1}}-4\mathbf{V^{n}}+\mathbf{V^{n-1}}}{2\Delta t}, \tag{13}$$

where the superscripts $n-1$, n and $n+1$ indicate three consecutive time levels, and $\Delta t=t^{n+1}-t^{n}=t^{n}-t^{n-1}$ represents the real time step. Thus, equations (8) – (12) can be expressed at the time level t^{n+1} in the form

$$\mathbf{V}^{n+1}+\sigma\mathbf{G}^{n+1}=\mathbf{F}^{n},\qquad D\mathbf{V}^{n+1}=0, \tag{14}$$

where $\sigma=2\Delta t/3$, $\mathbf{G}^{n+1}=\mathbf{G}\left(\mathbf{V}^{n+1},p^{n+1}\right)$ and $\mathbf{F}^{n}=\left(4\mathbf{V}^{n}-\mathbf{V}^{n-1}\right)/3$.

An iterative pseudo-time relaxation procedure with artificial compressibility is then used in order to advance the solution of the semi-discretized equations from the real time level t^{n} to t^{n+1} in the form

$$\frac{\partial\breve{\mathbf{V}}}{\partial\tau}+\breve{\mathbf{V}}+\sigma\breve{\mathbf{G}}=\mathbf{F}^{n},\qquad \delta\frac{\partial\breve{p}}{\partial\tau}+D\breve{\mathbf{V}}=0, \tag{15}$$

where $\breve{\mathbf{V}}(\tau)$ and $\breve{p}(\tau)$ denote the pseudo-functions corresponding to the variable velocity and pressure at pseudo-time τ, between the real time levels t^{n} and t^{n+1}, and δ represents an artificially-added compressibility.

An implicit Euler scheme is then used to discretize equations (15) between the pseudo-time levels τ^{ν} and $\tau^{\nu+1}=\tau^{\nu}+\Delta\tau$, and the resulting equations are expressed in terms of the pseudo-time variations $\Delta u=\breve{u}^{\nu+1}-\breve{u}^{\nu}$, $\Delta v=\breve{v}^{\nu+1}-\breve{v}^{\nu}$, $\Delta p=\breve{p}^{\nu+1}-\breve{p}^{\nu}$, in the matrix form

$$\left[\mathbf{I}+\sigma\Delta\tau\left(\mathbf{D}_X+\mathbf{D}_Y\right)\right]\Delta\mathbf{f}=\Delta\tau\,\mathbf{S}, \tag{16}$$

where $\Delta\mathbf{f}=\left[\Delta u,\Delta v,\Delta p\right]^{\mathrm{T}}$, $\sigma=2\Delta t/3$, $\boldsymbol{I}$ is the identity matrix, and where

$$\boldsymbol{D}_X=\begin{bmatrix} M+\dfrac{1}{\sigma} & 0 & C_7\dfrac{\partial}{\partial X} \\ 0 & M & C_4\dfrac{\partial}{\partial X} \\ \dfrac{C_7}{\sigma\delta}\dfrac{\partial}{\partial X} & \dfrac{C_4}{\sigma\delta}\dfrac{\partial}{\partial X} & 0 \end{bmatrix},\ \boldsymbol{D}_Y=\begin{bmatrix} N & 0 & C_2\dfrac{\partial}{\partial Y} \\ 0 & N+\dfrac{1}{\sigma} & C_3\dfrac{\partial}{\partial Y} \\ \dfrac{C_2}{\sigma\delta}\dfrac{\partial}{\partial Y} & \dfrac{C_3}{\sigma\delta}\dfrac{\partial}{\partial Y} & 0 \end{bmatrix},\ \boldsymbol{S}=\begin{bmatrix} F_u^n-\breve{u}^\nu-\sigma G_u^\nu \\ F_v^n-\breve{v}^\nu-\sigma G_v^\nu \\ -(1/\delta)\,D\breve{\boldsymbol{V}}^\nu \end{bmatrix}, \tag{17}$$

in which the differential operators M and N are defined as

$$M\phi=C_7\frac{\partial\left(\breve{u}^\nu\phi\right)}{\partial X}+C_4\frac{\partial\left(\breve{v}^\nu\phi\right)}{\partial X}+C_1\frac{\partial^2\phi}{\partial X^2}\ , \tag{18}$$

$$N\phi=C_2\frac{\partial\left(\breve{u}^\nu\phi\right)}{\partial Y}+C_3\frac{\partial\left(\breve{v}^\nu\phi\right)}{\partial Y}+C_6\frac{\partial^2\phi}{\partial Y\partial X}+C_5\frac{\partial^2\phi}{\partial Y^2}\ , \tag{19}$$

where ϕ can be Δu, Δv or Δp.

The optimal value of the artificial compressibility, δ, and the size of the pseudo-time step, $\Delta\tau$, are determined, as indicated in our previous papers [7, 8], based on the characteristic propagation velocity in the axial direction, $\lambda_+=\sigma q+\sqrt{(\sigma q)^2+\sigma/\delta}$, as

$$\delta=\frac{1}{2q^2\Delta\tau}\ ,\qquad \Delta\tau=\frac{C\,\Delta x}{\lambda_+}\ , \tag{20}$$

where q is a representative velocity of the unsteady flow, Δx is an average value of the mesh size and C is the Courant-Friedrichs-Levy number (between 30 and 40 is considered). The resulting values for δ and $\Delta\tau$ are eventually optimized by numerical experimentation.

A factored Alternating Direction Implicit (ADI) scheme is used to separate equation (17) into two successive sweeps in the Y and X directions, defined by equations

$$\left[\mathbf{I}+\sigma\Delta\tau\,\mathbf{D}_Y\right]\Delta\mathbf{f}^*=\Delta\tau\,\mathbf{S}\ ,\qquad \left[\mathbf{I}+\sigma\Delta\tau\,\mathbf{D}_X\right]\Delta\mathbf{f}=\Delta\mathbf{f}^*\ , \tag{21}$$

where $\Delta\mathbf{f}^*=\left[\Delta u^*,\Delta v^*,\Delta p^*\right]^{\mathrm{T}}$ is a convenient intermediate variable vector.

These equations are further spatially discretized by central differencing on a stretched staggered grid, in which the flow variables u, v and p are defined at different positions. By using a staggered grid, this method avoids the odd-and-even point decoupling while preserving the second-order accuracy in space of the method. The grid stretching is defined by hyperbolic sine functions in the X and Y directions.

A special decoupling procedure (Mateescu & Abdo [8]), based on the continuity equation, is used for each sweep to eliminate the pressure from the momentum equations.

The following relations, which are derived using equations (21) and (17) - (19) from the continuity equation expressed for each sweep,

$$\Delta p^*=-\frac{\Delta\tau}{\delta}\left[D\breve{\mathbf{V}}^\nu+C_2\frac{\partial\left(\Delta u^*\right)}{\partial Y}+C_3\frac{\partial\left(\Delta v^*\right)}{\partial Y}\right]\ ,\qquad \Delta p=\Delta p^*-\frac{\Delta\tau}{\delta}\frac{\partial\left(\Delta u\right)}{\partial X}\ , \tag{22}$$

are used to eliminate the pseudo-time variations of the pressure from the systems of equations for the pseudo-time variations of the velocity components in each sweep.

In this manner, the problem is reduced to the solution of two sets of decoupled scalar tridiagonal systems of equations, for each sweep. As a result, this method is characterized by excellent computational efficiency and accuracy.

3. METHOD VALIDATION FOR STEADY FLOWS PAST AIRFOILS WITH GURNEY FLAPS

The numerical method is validated by comparison with the results for steady flows obtained by Dumitrescu & Malael [13], the only published results for airfoils with Gurney flaps at low Reynolds numbers (no other numerical or experimental studies on airfoils with Gurney flaps at low Reynolds numbers are known). They used in their study a steady flow solver and restricted their computations to angles of attack smaller than 8 degrees; thus they did not find the oscillatory behaviour of the aerodynamic coefficients that is generated by the unsteady flow separations occurring at low Reynolds numbers (discussed further is the next section).

The present solution for the pressure coefficient distribution, C_p, along the upper and lower sides of a NACA 4404 airfoil with a Gurney flap of height $l = 2\%$ at the angle of attack $\alpha = 4^\circ$ and Reynolds number Re=1000 is compared in Figure 3 with the results obtained in [13]; a reasonable good agreement can be observed between these results.

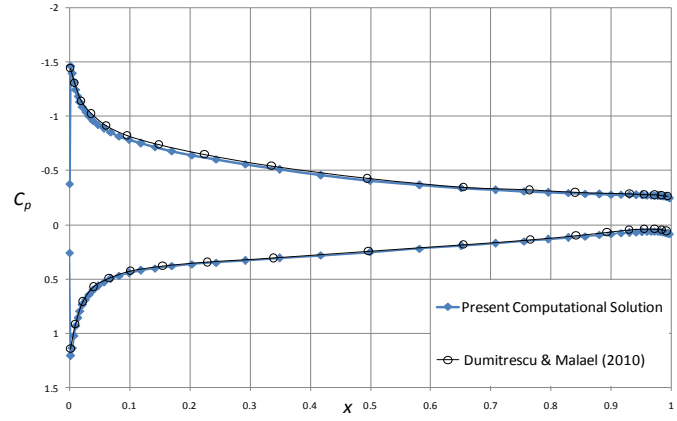

Figure 3. Method validation: Present solution for the pressure coefficient distribution, C_p, along the NACA 4404 airfoil with a Gurney flap of height $l = 2\%$ at $\alpha = 4^\circ$ and Re=1000, compared with the results obtained in [13].

The present solutions for the lift coefficient, C_L, and the lift-to-drag ratio, C_L/C_D, of a NACA 4404 airfoil equipped with a Gurney flap of height $l = 2\%$, at Reynolds number Re=1000, are also compared in Figure 4 with the results obtained in [13].

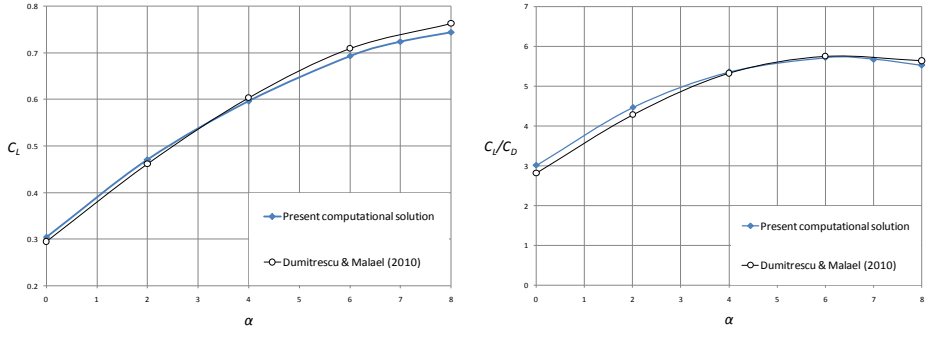

Figure 4. Method validation: Present solution for the variations with the angle of attack, α, of the lift coefficient, C_L, and the lift-to-drag ratio, C_L/C_D, of the NACA 4404 airfoil with a Gurney flap of height $l = 2\%$ at $\alpha = 4^\circ$ and Re=1000, compared with the results obtained in [13].

For steady flows, the influence of the Gurney flap height, l, on the lift and drag coefficients, C_L and C_D, is illustrated in Figure 5 for a NACA 0002 airfoil at Reynolds number Re=1000. One can notice that both C_L and C_D are increasing with the flap height l. However, the increase in the lift coefficient is much larger than the increase in drag, and thus the lift-to-drag ratio, C_L/C_D, is substantially increasing with the Gurney flap height, as it can be seen in Figure 6.

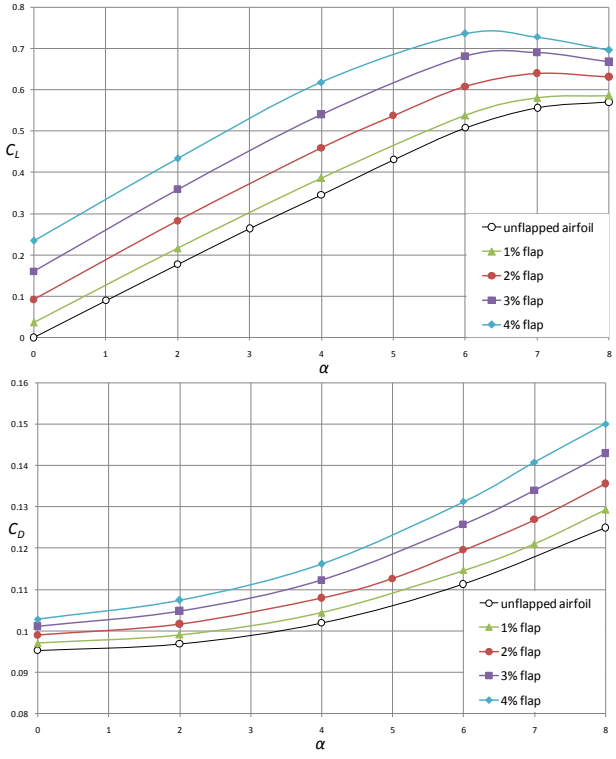

Figure 5. Influence of the Gurney flap height, l. Typical variations with the angle of attack, α, of the lift and drag coefficients, C_L and C_D, for the NACA 0002 airfoil at Re=1000 for various flap heights, from $l=0\%$ (airfoil without flap) to $l=4\%$.

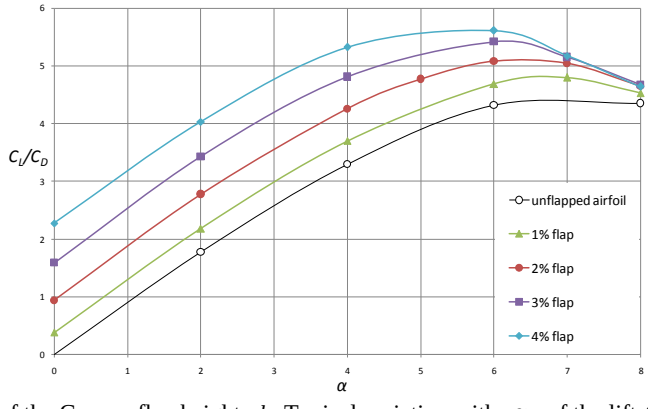

Figure 6. Influence of the Gurney flap height, l. Typical variation with α, of the lift-to-drag ratio, C_L/C_D, for the NACA 0002 airfoil at Re=1000 for various flap heights, from $l=0\%$ to $l=4\%$.

4. UNSTEADY EFFECTS ON AIRFOILS WITH GURNEY FLAPS DUE TO THE FLOW SEPARATIONS AT LOW REYNOLDS NUMBERS

The unsteady flow analysis indicates however that at larger angles of attack the flow past the airfoil becomes unsteady due to the unsteadiness of the flow separations occurring on the airfoil upper side at low Reynolds numbers. As a result, the aerodynamic coefficients of the airfoils with Gurney flaps, computed with the numerical method discussed, display oscillations in time at larger angles of attack. The typical variations with the non-dimensional time $t = t^* U_\infty / c$ (where t^* is the dimensional time) of the lift and drag coefficients, C_L and C_D, and of the lift-to-drag ratio, C_L/C_D, are illustrated in Figures 7 and 8 for the symmetric airfoil NACA 0004 equipped with a 2% Gurney flap ($l = 2\%$) at Reynolds number Re=1000 for various values of the angle of attack, α, in comparison with the same airfoil without flap ($l = 0\%$). One can notice that the lift and drag coefficients of the airfoil with Gurney flap display oscillations in time at incidences larger than $\alpha = 8^\circ$, and the oscillation amplitudes increase substantially with the angle of attack, α. The amplitudes of these oscillations of the aerodynamic coefficients, as well as their mean values are much larger than in the case of the same airfoil without flap.

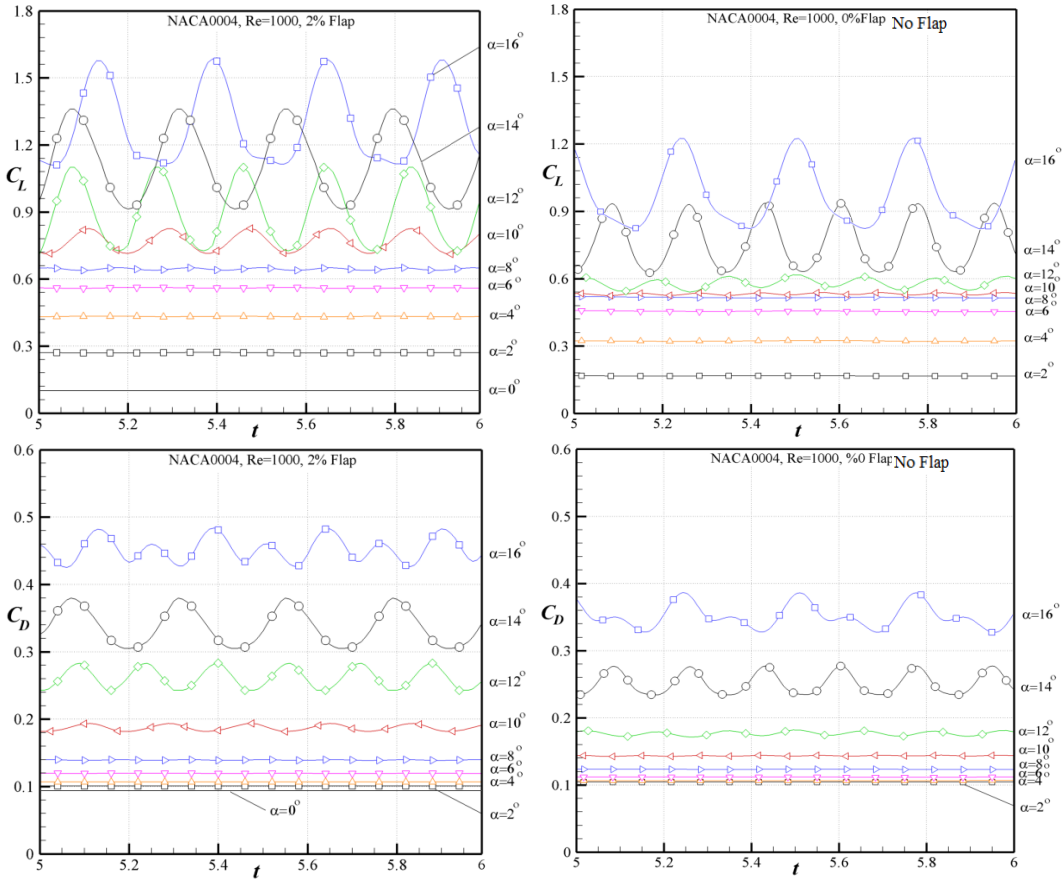

Figure 7. Typical time variations of the lift and drag coefficients, C_L and C_D, for the NACA 0004 airfoil with a 2% Gurney flap ($l = 2\%$) at Reynolds number Re=1000, for various values of the angle of attack, α, in comparison with the same airfoil without flap ($l = 0\%$).

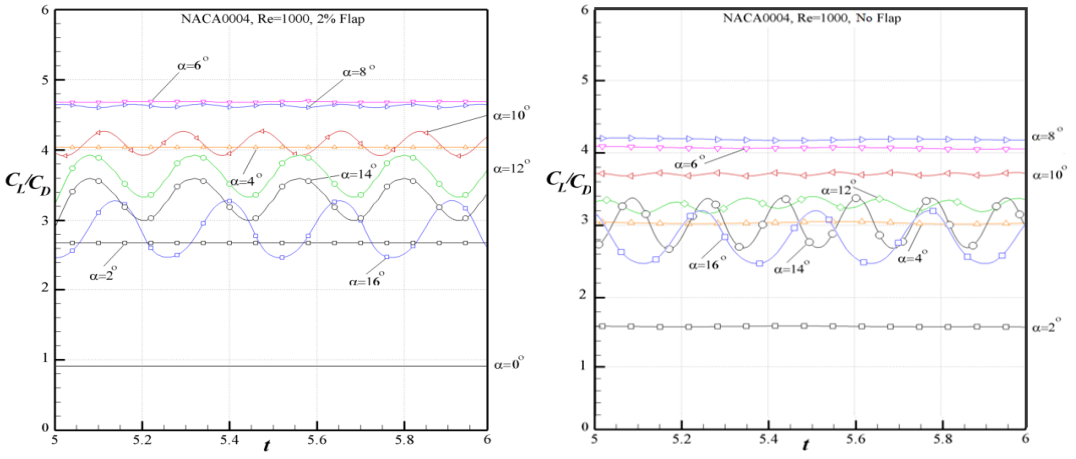

Figure 8. Typical time variations of the lift-to-drag ratio, C_L/C_D, for a symmetric NACA 0004 airfoil with a 2% Gurney flap ($l = 2\%$) at Reynolds number Re=1000, compared with the airfoil without flap ($l = 0\%$).

The periodic variations of the aerodynamic coefficients, which are illustrated in Figure 7, are consistent with the unsteady flow separation patterns illustrated by the flow visualizations shown in Figure 9 at several moments in time for the angle of attack $\alpha = 10^{\circ}$.

In this figure, the lines represent the streamlines of the flows, and the color shades indicate the local value of the non-dimensional flow velocity (with respect to the free stream velocity U_{∞}).

One can notice that the complexity of the unsteady flow separations increases with the increase in the angle of attack.

Influence of the Reynolds number

The influence of the Reynolds number can be seen by comparing the Figures 10, which present the variations with the nondimensional time $t = t^{*}U_{\infty}/c$ of the lift and drag coefficients, C_L and C_D, for the Reynolds numbers Re=600 and Re=1500, with the Figure 7 presenting the results for Re=1000.

One can notice that the amplitudes of oscillations of the aerodynamic coefficients, as well as their mean averages, increase substantially with the increase in the Reynolds number.

For Re=1500, the variations in time of the aerodynamic coefficients at the angle of attack $\alpha = 16^{\circ}$, although periodic, becomes more complex than a simple harmonic oscillation, which is due to the increase in the complexity of the unsteady flow separations with the increase in the angle of attack.

One can also notice that the stall conditions are reached in this case between $\alpha = 14^{\circ}$ and $\alpha = 16^{\circ}$, with the lift coefficient decreasing for $\alpha = 16^{\circ}$ while the drag coefficient is still increasing.

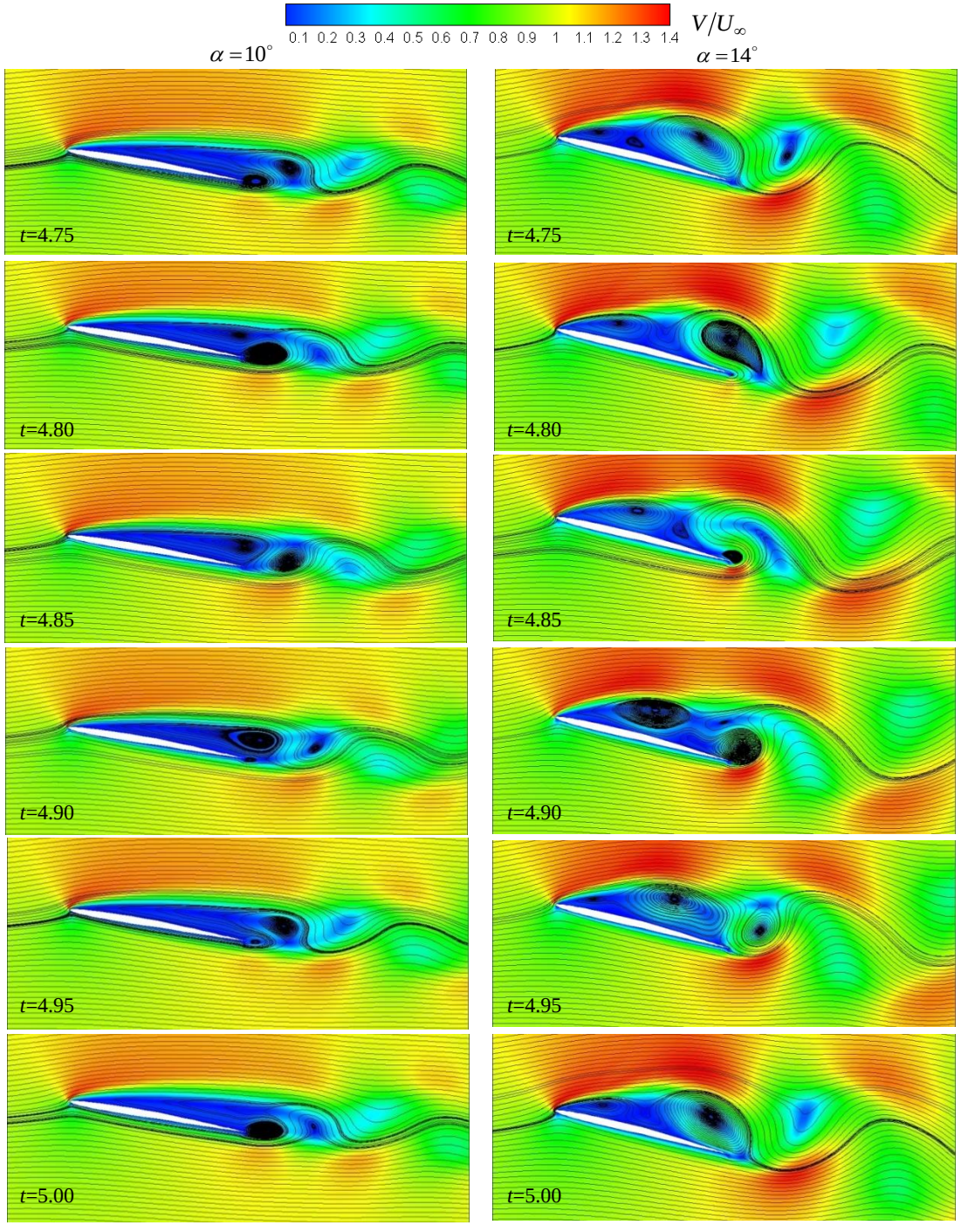

Figure 9. Illustration of the flow separations for NACA 0004 airfoil with a 2% Gurney flap ($l = 2\%$) at various moments in time for $\alpha = 10^\circ$ and $\alpha = 14^\circ$ at Reynolds number Re=1000. The lines are the streamlines and the color shades indicate the nondimensional velocity field (V/U_∞).

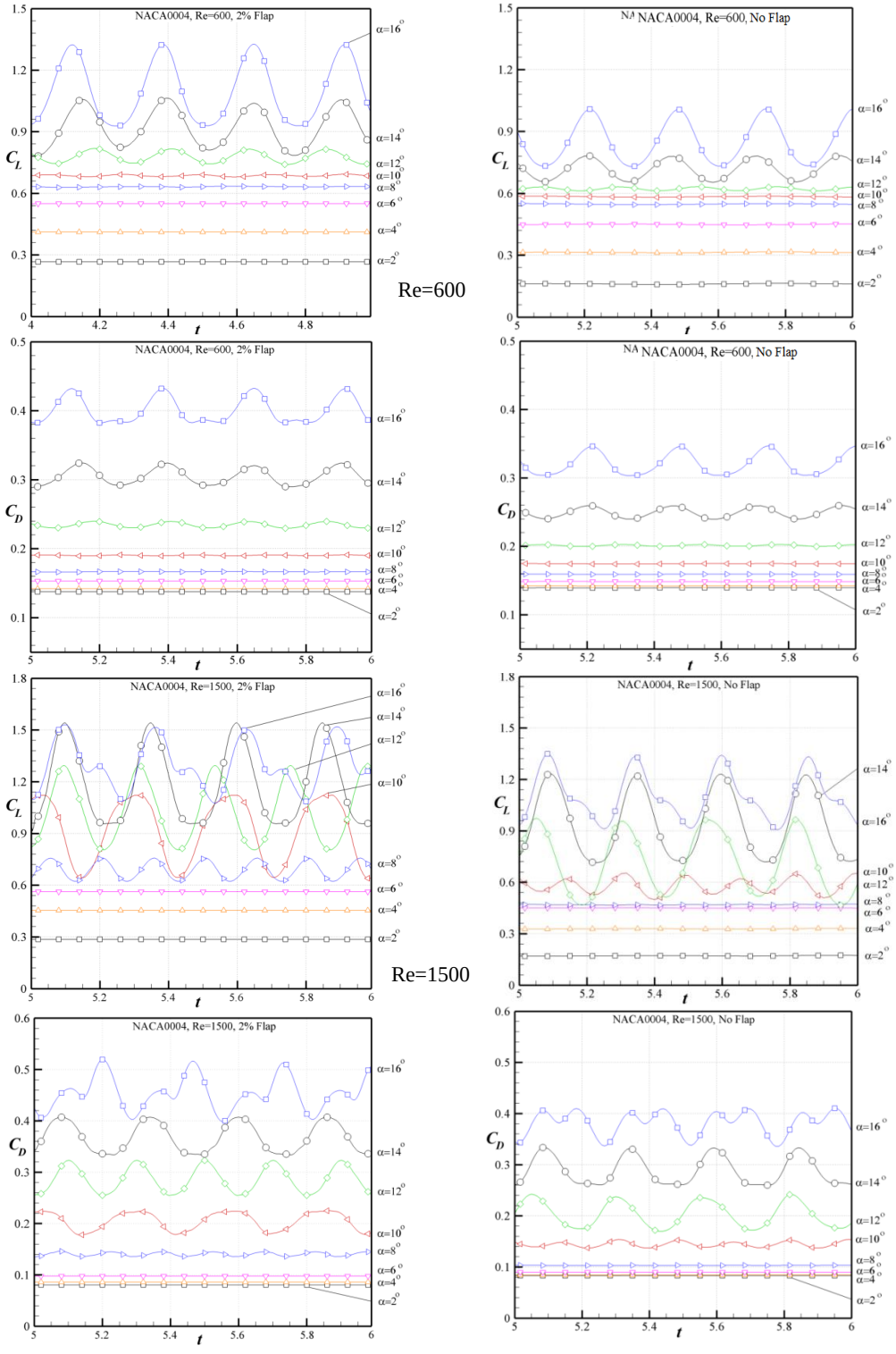

Figure 10. The time variations of the lift and drag coefficients, C_L and C_D, for the symmetric NACA 0004 airfoil equipped with a 2% Gurney flap ($l = 2\%$) at Reynolds numbers Re=600 and Re=1500, for various angles of attack, α, in comparison with the same airfoil without flap ($l = 0\%$).

Influence of the Gurney flap size

The influence of the Gurney flap height, l, is illustrated in Figure 11, which presents the variations with the non-dimensional time $t = t^* U_\infty / c$ of the lift and drag coefficients, C_L and C_D, for two values of the flap height, $l = 1\%$ and $l = 3\%$, at the Reynolds number Re=1000 and for various values of the angle of attack, α.

As expected, the lift and drag coefficients are both increasing with the increase in the height of the Gurney flap, l, but the lift coefficient is increasing more than the drag coefficient. As a result, the lift-to-drag ratio increases with the increase in the Gurney flap height from $l = 1\%$ to $l = 3\%$. The study of the effect of the Gurney flap height, l, can be extended by comparing Figure 10 with the results presented in Figure 7 for $l = 2\%$ and $l = 0\%$, which confirm the conclusions stated above.

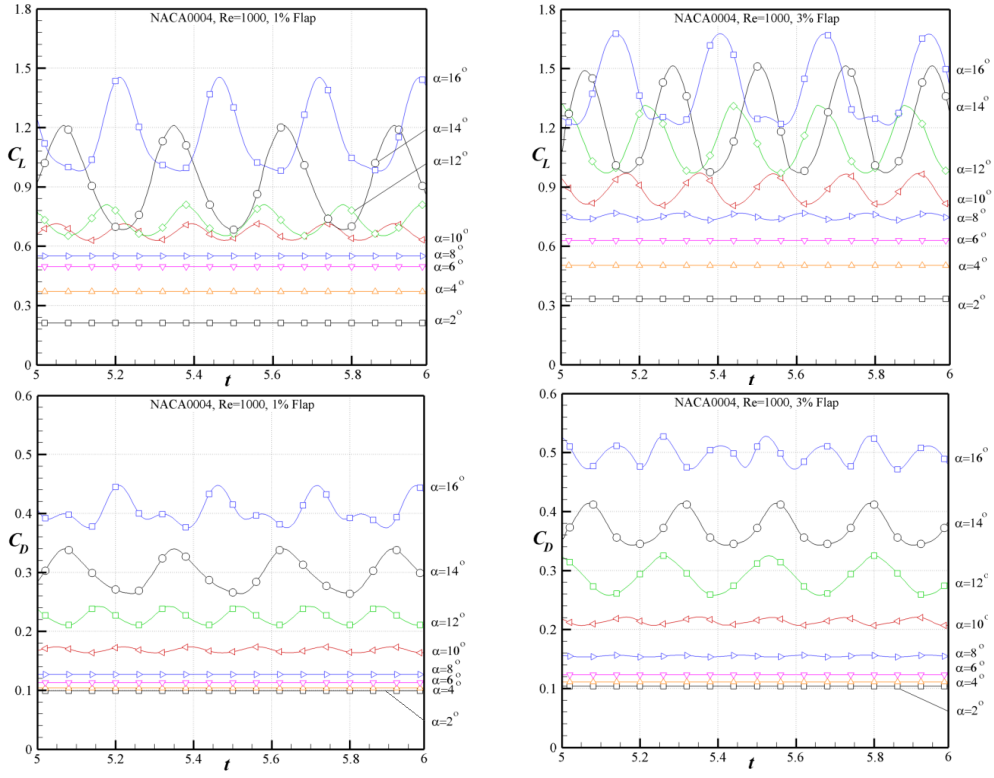

Figure 11. Influence of the Gurney flap height, l. The time variations of the lift and drag coefficients, C_L and C_D, for the symmetric NACA 0004 airfoil with a 1% Gurney flap ($l = 1\%$) at Reynolds number Re=1000, for various angles of attack, α, in comparison with a 3% Gurney flap ($l = 3\%$).

Influence of the airfoil thickness

The influence of the airfoil thickness is illustrated in Figure 12, which presents the variations with the non-dimensional time $t = t^* U_\infty / c$ of the lift and drag coefficients, C_L and C_D, for two symmetric airfoils, NACA 0002 and NACA 0004, equipped with 2% Gurney flaps at Reynolds number Re=1000 for various values of the angle of attack, α.

One can notice that the lift coefficient of the thinner airfoil is larger, leading to a slightly larger lift-to-drag ratio.

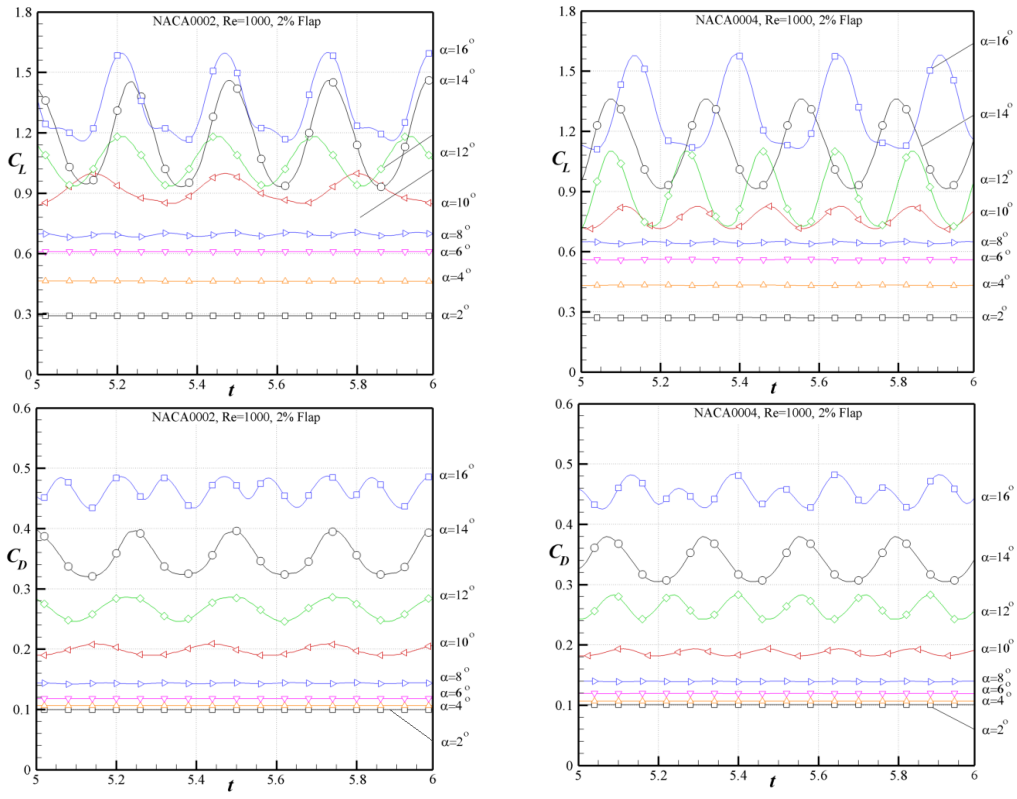

Figure 12. Influence of the airfoil thickness. The time variations of the lift and drag coefficients, C_L and C_D, for two symmetric airfoils, NACA 0002 and NACA 0004, with 2% Gurney flaps ($l = 2\%$) at Reynolds number Re=1000, for various angles of attack, α .

Unsteady flow solutions for cambered airfoils and the influence of the relative camber

Figure 13 shows the variations with the nondimensional time $t = t^* U_\infty / c$ of the lift and drag coefficients, C_L and C_D, for the cambered airfoil NACA 4404 equipped with a 2% Gurney flap ($l = 2\%$) at Reynolds number Re=1000 for various values of the angle of attack, α . In order to evaluate the influence of the relative camber, the results for the symmetric airfoil NACA 0004, of the same relative thickness and zero camber, equipped also with a 2% Gurney flap, are shown in the same figure for comparison. As expected, the lift coefficient of the cambered airfoil is larger than that of the symmetric airfoil with a Gurney flap of the same size, leading to a larger lift-to-drag ratio. One can notice that the oscillation amplitudes of the lift coefficient of the cambered airfoil are smaller than in the case of the symmetric airfoil for the same angle of attack.

The oscillatory behavior of the aerodynamic coefficients of lift and drag is consistent with the unsteady flow separation patterns illustrated by the flow visualizations shown in Figure 14 at several moments in time for the cambered airfoil NACA 4404 at two angles of attack, $\alpha = 10^\circ$ and $\alpha = 14^\circ$, and at Reynolds number Re=1000.

In these figures, the lines represent the streamlines of the flows, and the color shades indicate the local value of the nondimensional flow velocity (with respect to U_∞).

One can notice that the complexity of the unsteady flow separations increases substantially with the increase in the angle of attack.

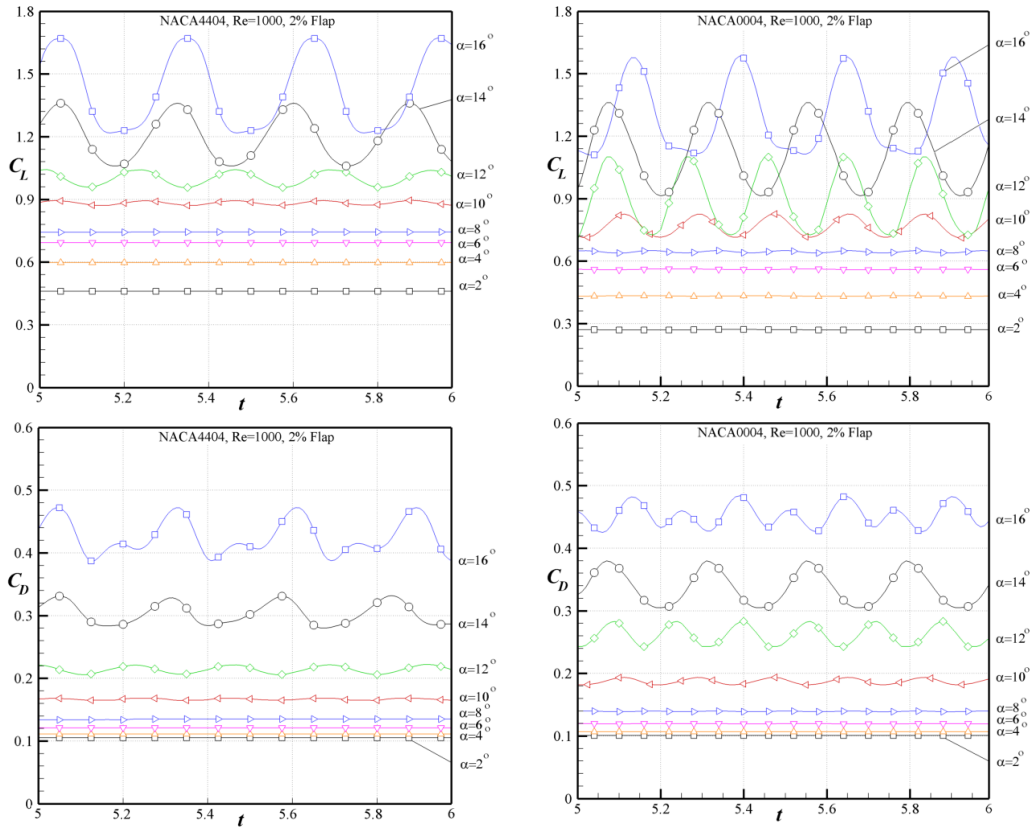

Figure 13. Typical time variations of the lift and drag coefficients, C_L and C_D, for a cambered NACA 4404 airfoil with a 2% Gurney flap ($l = 2\%$) at Reynolds number Re=1000, for various angles of attack, α, compared with the symmetric airfoil NACA 0004 with the same 2% Gurney flap.

5. CONCLUSIONS

This paper presents the unsteady flow analysis of the low-Reynolds-number flows past stationary airfoils equipped with Gurney flaps, aiming to study the unsteady behavior of the aerodynamic coefficients due to the flow separations occurring at these Reynolds numbers. This analysis is performed with an efficient time-accurate numerical method developed for the solution of the Navier-Stokes equations at low Reynolds numbers, which is second-order-accurate in time and space.

Solutions are presented in this paper for the aerodynamic coefficients of lift and drag and for the lift-to-drag ratio of several symmetric and cambered airfoils.

It was found that although the airfoil is considered stationary, starting from a relatively low incidence (about 8 degrees) the flow becomes unsteady due to the unsteadiness of the flow separations occurring at low Reynolds numbers, and the aerodynamic coefficients display periodic oscillations in time. The amplitudes of the aerodynamic coefficients oscillations increase with the angle of attack, and the unsteady flow separations become more complex (while remaining periodic) with a larger increase in the angle of attack.

A detailed study is presented in the paper on the influence of various geometric and flow parameters, such as the Gurney flap height, angle of attack, Reynolds number, airfoil relative thickness and relative camber, on the unsteady aerodynamic coefficients of lift and drag.

The flow separation is also studied with the aid of flow visualizations illustrating the changes in the flow pattern at various moments in time, by using the flow streamlines and the flow velocity field represented by color shades.

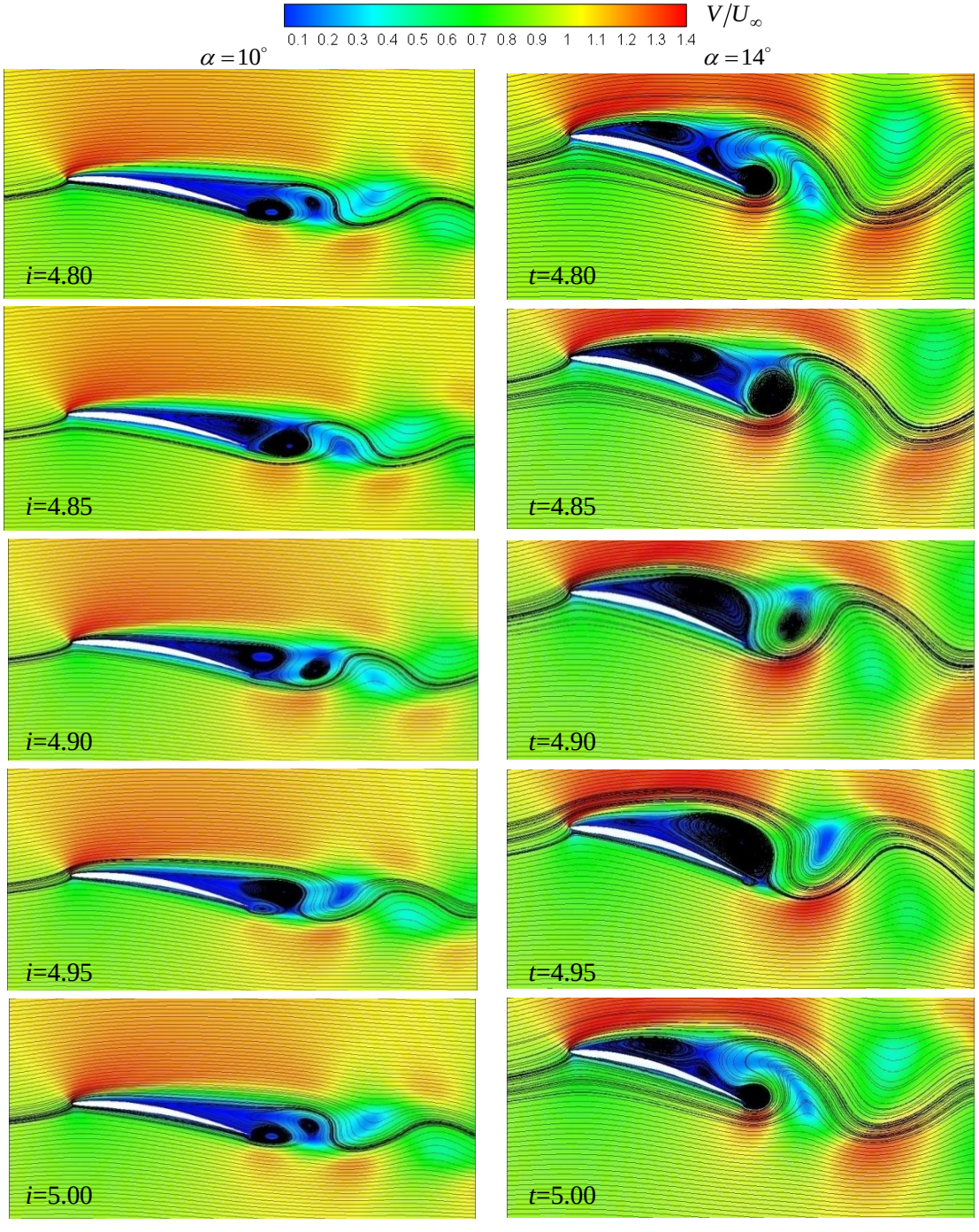

Figure 14. Illustration of the flow separations for NACA 4404 airfoil with a 2% Gurney flap ($l = 2\%$) at various moments in time for $\alpha = 10^\circ$ and $\alpha = 14^\circ$ at Reynolds number Re=1000. The lines represent the streamlines and the color shades indicate the non-dimensional velocity field (V/U_∞).

ACKNOWLEDGEMENT

The support of the Natural Sciences and Engineering Research Council of Canada (NSERC) is gratefully acknowledged, as well as the contributions of my graduate students A. Panahi and V. Roy.

REFERENCES

[1] R. Liebeck, Design of subsonic airfoils for high lift, *Journal of Aircrafts*, Vol. **15**, No. 9,1978, pp. 547-561.

[2] C. Jang, J. Ross & R. Cummings, Numerical investigation of an airfoil with a Gurney flap, *Aircraft Design I*, Vol. **1**, Issue 2, 1998, pp. 75-88.

[3] J. J Wang, Y. C. Li and K.-S. Choi, Gurney flap - Lift enhancement mechanisms and applications. *Progress in Aerospace Sciences*, Vol. **44**, Issue 1, 2008, pp. 22-47.

[4] T. Lee, Aerodynamics characteristics of airfoil with perforated Gurney-type flaps, *Journal of Aircrafts*, Vol. **46**, No. 2, 2009, pp.542-548.

[5] T. Lee & Y. Su, Pitching airfoil with combined unsteady trailing-edge flap deflection and Gurney flap, *AIAA Journal*, Vol. **50**, No.2, 2012, pp. 503-507.

[6] P. Kunz and L. Kroo, *Analysis and design of airfoils for use at ultra-low Reynolds numbers*, Proceedings of the AIAA Fixed, flapping and rotating wing aerodynamics at very low Reynolds numbers conference, Notre Dame, June 5-7, 2000, pp. 35-60.

[7] D. Mateescu and M. Abdo, *Aerodynamic analysis of airfoils at very low Reynolds numbers*, Applied Aerodynamics Conference, 42nd AIAA Aerospace Sciences Meeting, Reno, Nevad*a AIAA Paper* 2004-1053. Reno, Nevada, January 2004, pp. 1-11.

[8] D. Mateescu and M. Abdo, Analysis of flows past airfoils at very low Reynolds numbers, *Journal of Aerospace Engineering*, Vol. **224**, 2010, pp. 757-775.

[9] D. Mateescu, O. Scholz and C. Wang, Aerodynamics of airfoils at low Reynolds numbers in the proximity of the ground, *12th Pan American Congress of Applied Mechanics - PACAM XII*, Port of Spain, Trinidad, 2-6 January 2012, Paper # 203, pp. 1-6.

[10] D. Mateescu, M. Munoz and O. Scholz, Unsteady Flows past Oscillating Airfoils at Low Reynolds numbers, 29th Applied Aerodynamics Conference, Honolulu, Hawaii, June 2011, *AIAA Paper 2011-3657*, pp. 1-15.

[11] D. Mateescu, A. Panahi, C. Wang and O. Scholz, *Analysis of steady and unsteady flows past airfoils in the proximity of the ground at low Reynolds numbers*, 30th Applied Aerodynamics Conference, New Orleans, Louisiana, June 2012, *AIAA Paper* 2012-3028, pp. 1-20.

[12] D. Mateescu, A. Panahi & C. Wang, Unsteady effects on stationary airfoils due to unsteady flow separations at low Reynolds number, *31st AIAA Applied Aerodynamics Conference*, San Diego, California, June 2013. AIAA Paper 2013-2527, pp. 1-30.

[13] H. Dumitrescu & I. Malael, Analysis of low Reynolds number flow past Gurney flap, *INCAS BULLETIN*, *(*online) ISSN 2247–4528, (print) ISSN 2066–8201, ISSN–L 2066–8201, Vol. **2**, No. 4, DOI: 10.13111/2066-8201.2010.2.4.14, 2010, pp. 97-105.

[14] D. Mateescu, A Panahi and V. Roy, Analysis of three-dimensional confined laminar flows with multiple flow separation regions, *Applied Aerodynamics Conference*, 50th *AIAA Aerospace Sciences Meeting*, Nashville, Tennessee, 9-12 January 2012, *AIAA Paper* 2012-0703, pp. 1-13.

[15] D. Mateescu, A. Panahi, Analysis of unsteady three-dimensional confined flows with oscillating walls and variable inflow velocity, 51st *AIAA Aerospace Sciences Meeting*, *AIAA Applied Aerodynamics Conference*, Grapevine, Texas, USA, 7-10 January 2013, AIAA Paper 2013-0063, pp. 1-18.

[16] D. Mateescu and M. Abdo, Efficient second-order analytical solutions for airfoils in subsonic flows, *Aerospace Science and Technology Journal*, 2005, Vol. **9**, pp. 101-115.

[17] D. Mateescu and M. Abdo, Nonlinear theoretical solutions for airfoil aerodynamics, 21st Applied Aerodynamics Conference, Orlando, Florida, June 2003, *AIAA Paper 2003-4296*, pp. 1-16.